Hindawi
Advances in Civil Engineering
Volume 2020, Article ID 9168908, 13 pages
https://doi.org/10.1155/2020/9168908

Research Article

The Meso-Analysis of the Rock-Burst Debris of Rock Similar Material Based on SEM

Manqing Lin,[1] Lan Zhang ,[1] Xiqi Liu ,[2] Yuanyou Xia,[2] Jiaqi He,[1] and Xiaosu Ke[1]

[1]*School of Xingfa Mining Engineering, Wuhan Institute of Technology, Wuhan, Hubei 430062, China*
[2]*School of Civil Engineering and Architecture, Wuhan University of Technology, Wuhan, Hubei 430070, China*

Correspondence should be addressed to Lan Zhang; zlgzzh6@163.com and Xiqi Liu; liuxx142857@163.com

Received 28 April 2019; Revised 25 July 2019; Accepted 12 February 2020; Published 3 April 2020

Academic Editor: Cumaraswamy Vipulanandan

In order to explore the specimen failure characteristics during rock-burst under different gradient stress conditions, in this paper, a novel experimental technique was proposed; a common series of tests under two gradient stress paths were conducted on rock similar material specimens using the true-triaxial gradient and hydraulic-pneumatic combined test apparatus. And plaster was used as the rock similar material. In the experimental process, several rock-burst debris with area sizes of 100 mm^2 were collected, and the fractal dimensions of typical detrital section crystal contours were analyzed and calculated using a scanning electron microscopy (SEM) method. The results showed that the specimens' failure characteristics which had been induced by the two gradient stress processes were various. Also, the mesoscopic morphology of the rock-burst detrital section had effectively reflected its macroscopic failure characteristics. It was found that the fractal dimensions of the crystal contours of the specimen's detrital section had fractal characteristics, and the box-counting dimension based on the SEM image could quantitatively describe the rock-burst failure characteristics. Furthermore, under the same magnification, the fractal dimensions of the crystal contours of the splitting failures were found to be relatively smaller than those of the shearing failures.

1. Introduction

At the present time, with the gradual shortages in shallow mineral resources of the Earth, the annual global demand resource gap has increased, and the mining of mineral resources has gradually developed to deeper underground spaces. The occurrence environments of deep rock masses are extremely complex, and the stress concentrations in the surrounding rock of deep mining operation often lead to the sudden release of stored elastic energy after excavation activities, which subsequently result in rock-burst disasters [1]. When rock-burst occurs, it is mainly manifested as rock masses breaking away from the parent rock formations with large amounts of kinetic energy. These actions throw debris at the freeing excavation surfaces, which are accompanied by explosions and tearing sounds of different degrees. This often leads to the destruction of mining machinery, or even death to miners, and brings immeasurable losses to the mining projects [2, 3]. Therefore, the study of rock-burst phenomena is helpful to increase the understanding of rock-burst, which may lead to the effective prevention of their occurrences in the future.

The macroscopic failure phenomena of rock masses are full expressions of many mesoscopic fractures [4, 5]. The mesoscopic study of the rock-burst phenomena will be helpful for further understanding the failure processes of rock-burst. Generally speaking, researchers usually use scanning electron microscopy (SEM) to determine the mechanical properties of rock masses in order to reveal the relationship between the mesoscopic morphology of the rock and the failure process. Previously, Zhao et al. [6] analyzed the microstructures of sections rock masses which had undergone rock-burst using SEM and revealed the dynamic failure mechanism of rock. Also, Ng et al. [7–9] processed the scanning images of research material using an electron microscope and established a model to predict crack growth. In another related study, Zhang et al. [10] detected the microstructures and mineral compositions of different

shallow rock specimens using SEM and then analyzed the influences of the different microstructures and mineral compositions on the macroscopic mechanical properties. However, there are currently few reports available regarding the study of rock-burst clastic fractures. The application of SEM to the study of rock-burst mesostructure will potentially be helpful in increasing the understanding of the failure mechanisms related to rock-burst phenomena.

Fractal theory was proposed by Parsa et al. [11] to study complex nonlinear science. It has been found that, in the field of rock mass mechanics, since Fujimura et al. [12] applied the fractal theory to study the fractal dimensions of rock detrital sectional images, the application of fractal theory in image fields has become increasingly mature. Wang et al. [13] adopted a fractal method to quantitatively describe the failure evolution behavior of microcracks in rock masses. Also, based on fractal methods and fracture mechanics theories, Deng et al. [14] established an energy consumption model for rock fractures and obtained the quantitative relationship between the energy consumption and the average sizes of rock debris. The results mentioned above showed that the fractal theory could be used to describe the characteristics of rock fractures quantitatively. It has been determined that rock-burst mainly occurs in hard and brittle rock masses. Therefore, the cross sections and debris which are produced by rock-burst are known to be closely related to the characteristics of the rock-burst. In the field of rock-burst research, the majority of the research methods utilize the calculations of the fractal dimensions, which are based on the measurements of the masses, lengths, widths, and other scales of the rock-burst debris [15–17], and then judge the severity of rock-burst phenomena based on the acquired fractal dimensions.

Therefore, the current study used a rock-burst test device with the true-triaxial gradient and hydraulic-pneumatic combined test device which had been independently developed to carry out rock-burst tests on rock similar material specimens under two stress loading modes: uniform distribution and gradient distribution. Then, based on the macroscopic failure analyses of the rock-burst, the influences of the uniform loading and gradient loading on failure characteristics of the specimens were analyzed from a mesoscopic perspective by selecting typical failure section samples and using SEM. Also, by further combining the results with MATLAB software calculations, it was determined in this study that a debris fractal rule had existed under the different rock-burst failure modes in the cross sections of the specimens. The results of this study have potentially important theoretical significance for deepening the understanding of rock fracture characteristics and the influencing factors of rock-burst phenomena in surrounding rock masses during excavation activities.

2. Testing of the Rock-Burst Phenomena

2.1. Test Device and Materials. The true-triaxial gradient and hydraulic-pneumatic combined test device which was adopted in this study's testing process was composed of the host, hydraulic control system, and pneumatic control system, as detailed in Figure 1. Also, the device had the ability of realizing two-dimensional and three-dimensional confining stress loading. The maximum loading capacity on the top of the device was 20 MPa, and the maximum loading capacity on the side of the device is 5 MPa. The gradient setting at the top of the device had simulated the stress concentration phenomena of deep rock masses caused by excavation disturbances in the field. Moreover, the pneumatic control system was able to effectively simulate the soft loads imposed by the surrounding rock during rock-burst processes in deep rock masses under actual conditions.

Due to the complex processing and transportation actions of the natural rock specimen and the limitations of the laboratory tests, this study selected high-strength plaster as the material. The plaster specimens were found to meet the rock-burst proneness indexes of rock and had displayed similarities in mechanical properties to deep rock masses [18–20]. The parameters of the plaster are shown in Table 1. Then, in accordance with the spatial arrangement of the specimen loading chamber in the test device, the sizes of the specimens were set as 1,000 mm × 600 mm × 400 mm. Also, in order to reduce the influences of lateral friction on the loading processes of the specimen, two layers of polytetrafluoroethylene (PTFE) film were placed between the loading surfaces of the specimen and the force transfer plate of the instrument. Then, a layer of graphite powder was also applied on the surfaces of the specimens.

2.2. Test Process. This study test process had mainly simulated the rock-burst phenomena caused by engineering disturbances, such as the sudden unloading of excavation surfaces during deep rock mass excavations. At present, it is generally believed that the small size specimens used in rock-burst tests suffer uniform loading and only undergo splitting failure. However, this is different from rock-burst phenomena in some sites. It was found that the gradient stress loading method can better reflect the phenomenon of tangential stress concentration in rock-burst site during tunnel excavation. In the current study, the simplified expression of $y = ae^{-bx} + c$ [21] formula was used in underground excavations. It was observed that the tangential stress of the surrounding rock of the cavern within a certain distance had decreased with the increasing of the width of the horizontal distance. In the formula, $a + c$ is located at the direction of the tangential stress of the surrounding rock tunnel wall; b represents the stress gradient coefficient (the larger the b is, the greater the stress differences are at the top of the gradient); x is the surrounding rock in some point to the width of the horizontal distance; and c denotes the initial stress value.

In order to compare and analyze the effects of uniform loading and gradient loading on the characteristics of rock-burst, this paper designed two test loading modes to conduct multiple tests on large specimens. The stresses of plaster specimens are shown in Figure 2.

During the testing, the initial confining pressure of the plaster specimens was set as 1.5 MPa ($c = 1.5$ Mpa), and the loading was graded at 0.5 MPa for each stage. The loading

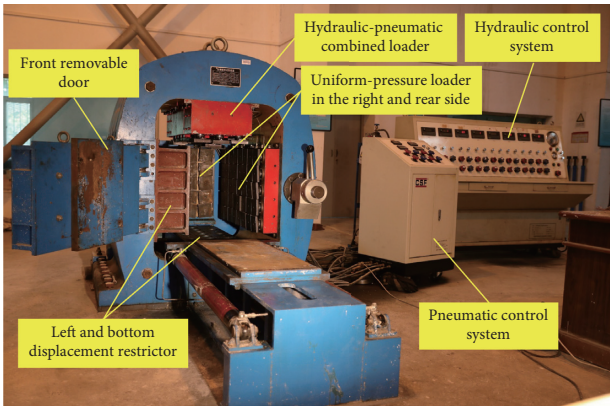

Figure 1: YB-A type pneumatic-hydraulic composite rock-burst simulation test device.

Table 1: Parameters of the specimen material.

Material	Water/plaster ratio	UCS (MPa)	Impact energy index	Density (g·cm^{-3})
Plaster	0.6	9.2	5.8	2.1

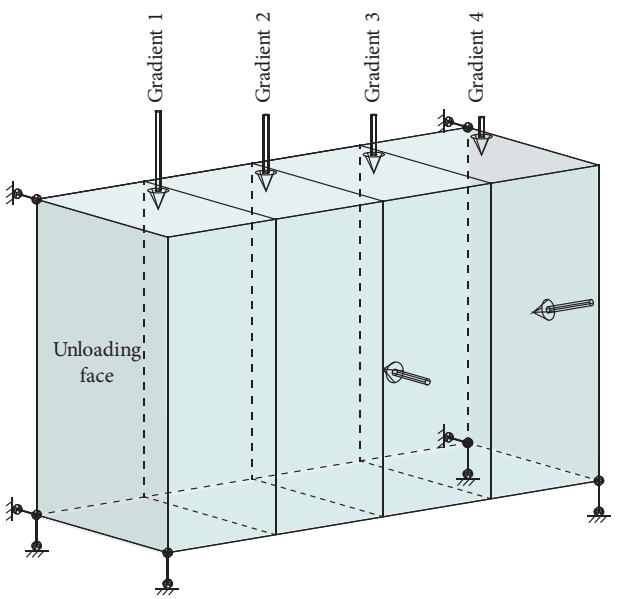

Figure 2: Diagram of the simulated forces of the specimens.

interval for each stage was 30 minutes, and the initial confining pressure was stabilized for a period of 6 hours. Then, the limiting door plate in front of the device was quickly evacuated. Meanwhile, at the top, the load is calculated by $y = ae^{-bx} + c$. The x value of gradient 1 is 0 m, the x value of gradient 2 is 0.25 m, the x value of gradient 3 is 0.50 m, and the x value of gradient 4 is 0.75 m. The initial value of a is 0.5 MPa, and the interval in each loading is 0.5 MPa. The stress loading scheme of the experimental design was as follows.

(1) Uniform stress loading: the loading path of this scheme is shown in Figure 3(a). When $b = 0$, the top Gradient 1 was loaded in a gradient of 0.5 MPa, and the top of the other gradients was calculated as $y = ae^{-bx} + c$ and loaded until rock-burst had occurred.

(2) Gradient stress loading: the loading path of this scheme is shown in Figure 3(b). When $b = 6$, the top Gradient 1 was loaded in a gradient of 0.5 MPa, and the top of the other gradients was calculated as $y = ae^{-bx} + c$ and loaded until rock-burst had occurred.

2.3. Test Results

2.3.1. Analysis of the Test Phenomena. Figures 4 and 5 show the macroscopic rock-burst failure phenomena which had been caused by uniform loading test and gradient loading test, respectively. According to the different loading paths, the characteristics of the phenomena, such as the stress loading threshold, rock-burst form, blasting sounds, and debris ejections during rock-burst test, were analyzed.

The details of the analysis results were as follows.

(1) In terms of test stress loading conditions, in the process of uniform loading test, rock-burst occurred when the top load increased to 5.5 MPa, and the upper parts of the specimens were destroyed, as shown in Figure 4(a). In the process of gradient loading test, rock-burst occurred in the upper and middle part of the specimen when the loads on the top Gradient 1 had increased to 5.0 MPa, as detailed in Figure 5(a). It could be seen that the stress of the specimens under the uniform loading conditions was greater than those under the gradient loading conditions.

(2) In terms of the sounds which had occurred at the times of the rock-burst, it was observed that the rock-burst occurring under the uniform loading conditions had produced continuous, crisp, and low

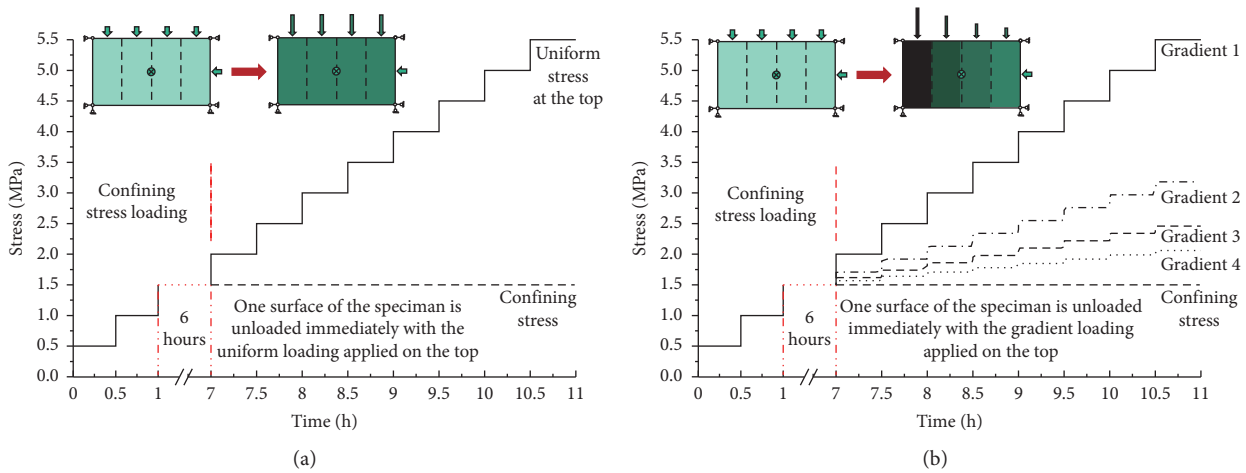

Figure 3: Stress loading paths of the specimens: (a) uniform stress loading; (b) gradient stress loading.

Figure 4: Phenomena of the uniform loading test: (a) rock-burst moment; (b) after the rock-burst; (c) rock-burst pit; (d) side cracking of the specimen.

Figure 5: Phenomena of the gradient loading test: (a) rock-burst moment; (b) after the rock-burst; (c) rock-burst pit; (d) side cracking of the specimen.

sounds. Meanwhile, the rock-burst which occurred during the gradient loading test had produced very loud and dull sounds.

(3) In terms of the failure modes of the rock-burst phenomena, the closely observed fractures which had occurred during uniform loading of the specimens and after the rock-burst had occurred are shown in Figures 4(c) and 4(d). It was found that the rock-burst sections were relatively rough and the surfaces of the formed rock-burst pits were flat. Also, the side cracks had expanded along the direction of the loading stress. The gradient stress loading specimen's sections of the rock-burst were found to be relatively smooth, and the formations of the pits

were observed to be wedge-shaped. The rock-burst could be seen from the side close to 45° angle shear cracks, where large amounts of plaster powder had remained within the cracks.

(4) In terms of the debris generated by the rock-burst, it can be seen from Figure 4(b) that, following the rock-burst under the uniform loading, large amounts of plate-like debris were concentrated within the range of 0.5 m. However, when the rock-burst occurred under the gradient loading, the debris had dispersed, with debris even thrown beyond a 1 m range. Therefore, it was concluded in this study that the rock-burst debris which had been generated under the gradient loading was stronger than that under the uniform loading conditions.

It can be seen from the above-mentioned results that, during the uniform loading test, the rock-burst had occurred for long periods of time with low sound. Also, the rock-burst sections were flat; the cracks were typical splitting cracks; and the rock-burst intensity was weak. However, during the gradient loading test, the durations of the rock-burst were short; the rock-burst pits were wedge-shaped; the cracks were typical shear cracks; and the rock-burst intensity was strong. Therefore, this study results had indicated that the rock-burst characteristics produced by the uniform loading test and gradient loading test were obviously different.

2.3.2. Macroscopic Detrital Features. In the current study, in order to further examine the failure characteristics generated by the different loading methods, two groups of test debris were classified according to particle sizes and types. In other words, each group of test debris was divided into 10 groups according to size as follows: <3 mm; 3 to 6 mm; 6 to 10 mm; 10 to 20 mm; 20 to 25 mm; 25 to 40 mm; 40 to 70 mm; 70 to 100 mm; 100 to 160 mm; and >160 mm. Each group was divided into two subgroups according to block and sheet. The debris with the length to thickness ratio less than 3 were block, while those with the length to thickness ratio more than 3 were sheet [17, 22], as shown in Figure 6.

As can be seen from Figure 6, more debris had been formed during the uniform loading, while less debris had formed during the gradient loading. Therefore, in order to determine the percentage of the different types and sizes of detritus in the total detritus, after classifying the detritus and adding their masses, the percentages of the detritus mass of the rock-burst under the different stress loading conditions are detailed in Table 2.

As detailed in Table 2, under the uniform loading conditions, the mass percentages of the sheet debris were 47.42%, 11.65%, 12.89%, 2.51%, 2.32%, and 1.98%, respectively, for a total of 78.77%, which was far higher than the mass percentage of block debris. However, under the gradient loading conditions, it was observed that, contrary to the uniform loading results, the masses of the block debris had accounted for more than 70% of the total mass. Therefore, it was determined that the rock-burst generated by the uniform loading had produced mainly sheet debris, and the rock-burst generated by the gradient loading had resulted in mainly block debris.

In the current study, by comparing the characteristics of the samples' debris and affected sections following the tests, it was ascertained that, under the uniform loading test conditions, the rock-burst had generated less sound; the rock-burst pits were flat; the highest percentage of the debris was in the form of plates and sheets; the sections were rough; and the cracks had expanded along the loading direction. However, the rock-burst sounds produced by the specimens under gradient loading were louder; the rock-burst pits were wedge-shaped; the debris was mainly massive; the cracks were mainly shear line cracks; and the sections were covered with rock powder and scratches. Therefore, from a macroscopic point of view, the uniform loading test could be concluded to have mainly resulted in split failures, while the gradient loading test had mainly resulted in shear failures of the rock similar material specimens.

3. Mesoscopic Analysis of Rock-Burst Sections of Rock Similar Material

The mesoscopic analysis of rock can be studied with the aid of SEM. In accordance with the results of the SEM study conducted by Tian [23], in rock-burst sections of underground chambers, the rock crystals tend to have regular geometric shapes, and the scanning images of fracture sections which have been formed by different loading methods have been found to be obviously different. Although the crystal structures inside the rock and plaster were different, the crystals inside the plaster were found to be regularly distributed under the conditions of no stress, which was similar to the crystal structures inside the rock. Therefore, it could be inferred that the scanning images of rock-burst detrital sections of the rock similar material formed by the different loading modes would also have obvious differences.

3.1. SEM Testing of the Detrital Sections of the Rock Similar Material

3.1.1. SEM Sampling of the Detrital Sections. In order to observe the failure characteristics of the rock similar material under different stress gradient loading conditions from a mesoscopic perspective, the samples were divided into two groups. The first group is the splitting failure section in the uniform loading test, as shown in Figure 7(a). The second group is shear failure section in gradient loading test, as detailed in Figure 7(b). Three samples were collected for each test group [24].

Then, for the purpose of meeting the requirements of the SEM equipment for sample sizes, approximate rectangular cutting was first carried out on the rock-burst detrital section [25]. The sample area was approximately 10 mm × 10 mm, with a thickness ranging between 3 and 5 mm, and the back area was worn flat. The cut test samples are shown in Figures 7(a) and 7(b). The images denoted by No. 1, No. 2, and No. 3 indicate the samples of the splitting failure

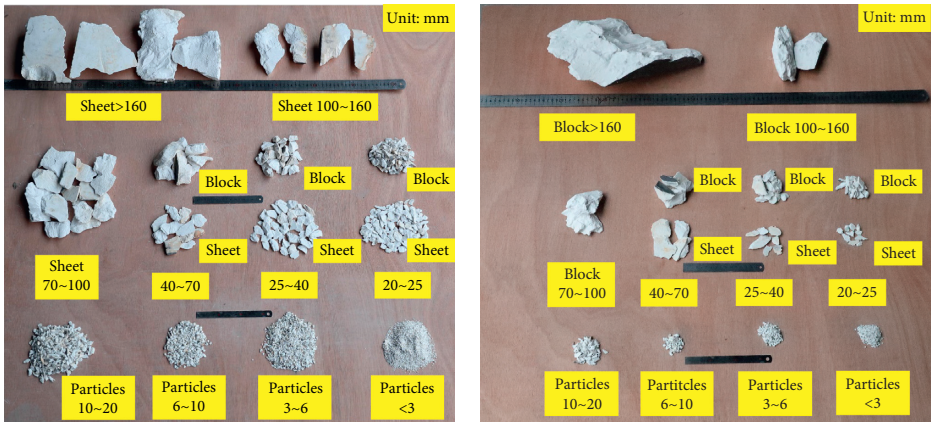

Figure 6: Typical debris classification diagram: (a) uniform loading test debris; (b) gradient loading test debris.

Table 2: Different debris mass percentages under the different stress loading conditions.

Size (mm)	Form	Uniform loading		Gradient loading	
		Quality (g)	Percentage (%)	Quality (g)	Percentage (%)
>160	Sheet	1.140	47.42	—	—
	Block	—	—	1.100	70.39
100 to 160	Sheet	280	11.65	—	—
	Block	—	—	225	14.4
70 to 100	Sheet	310	12.89	—	—
	Block	—	—	80.7	5.16
40 to 70	Sheet	51.7	2.15	27.3	1.75
	Block	168.1	6.99	52.8	3.38
25 to 40	Sheet	55.8	2.32	8.1	0.52
	Block	78.9	3.28	28.8	1.84
20 to 25	Sheet	47.5	1.98	2.8	0.18
	Block	74.3	3.09	14.3	0.91
<20	Particles	197.9	8.23	22.9	1.47
Total	—	2,404.20	100	1,562.70	100

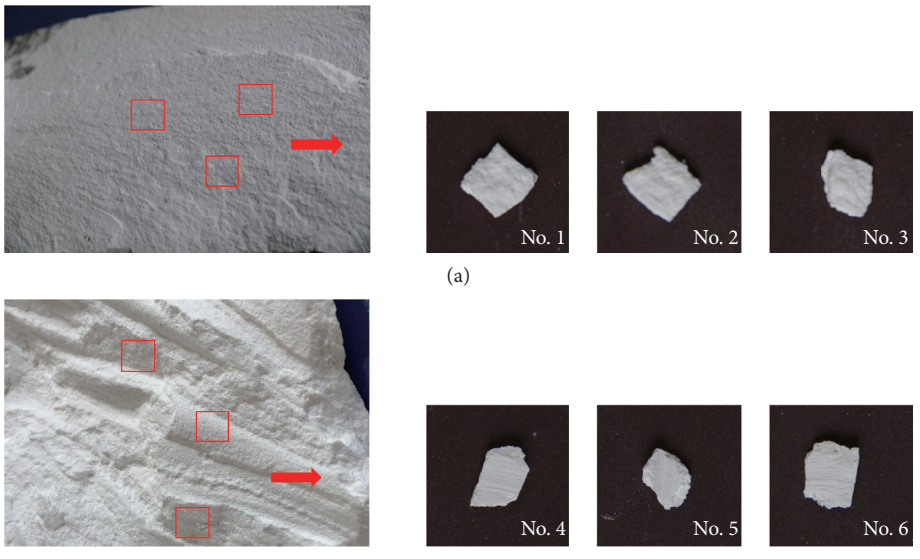

Figure 7: Failure modes of the typical samples and debris under the different stress gradients: (a) splitting failure surface and sample diagram; (b) shear failure surface and sample diagram.

surfaces (Figure 7(a)) under the uniform loading conditions; and No. 4, No. 5, and No. 6 images indicate the samples of the shear failure surfaces (Figure 7(b)) under the gradient loading conditions.

3.1.2. Test Equipment and Testing Process. The samples were successively fixed on a sample table with conductive adhesive. Then, in order to increase the conductivity of the samples and enhance the emissivity of the signals, vacuum gold-plating film was applied [26]. After gold plating, the samples were observed by Japanese jsm-5510lv scanning electron microscope with magnification of 50–2000 times.

3.1.3. Mesoscopic Morphology Features of the Rock-Burst Sections. SEM images of the typical detrital sections in the above-mentioned two groups of samples were selected. Figures 8(a) and 8(b) show the SEM images of the splitting failure detrital sections selected in the uniform loading test, and Figures 9(a) and 9(b) show the SEM images of the shear failure detrital sections in the gradient loading test.

Although the SEM image is a two-dimensional photograph, it contains a lot of three-dimensional information. For example, the image can clearly show the size, three-dimensional morphology, and distribution of plaster crystal and gap. The mesostructure information is reflected by the gray value. Each pixel corresponds to a grayscale value ranging from 0 to 255 (0 for black and 255 for white). Different gray values can be understood as different distances between the crystal surface and the imaging surface. The larger the gray value is, the closer the crystal surface is to the imaging surface. According to this principle, two groups of experimental SEM images can be selected and programmed with MATLAB to convert two-dimensional SEM images into three-dimensional grayscale images, as shown in Figures 8(c) and 9(c).

The observational results were as follows.

(1) Following the uniform loading test, the surfaces of the rock-burst detrital sections were observed to be generally loose, with pits and pores distributed throughout, as illustrated in Figure 8(a). Then, after a local magnification of 300 times, it was found that the majority of the crystals were slender and long in appearance, and the intact crystal shapes could be clearly seen. The pores were also more obvious, and the crystals were found to overlap irregularly around the pores, as can be seen in Figure 8(b).

(2) Following the completion of the gradient loading test, the plaster crystals squeezed by shear failure in the gradient loading mode result in a relatively dense state compared with the crystals in the uniform loading mode, accompanied by obvious scratches and steplike patterns perpendicular to the direction of scratches, as detailed in Figure 9(a). Once again, following a magnification of 300 times, the majority of the detrital sections were found to be flat, and most of the plaster crystals were observed to be short and rod-like ones. The main failure mode was determined to be the transgranular fractures, with partial steplike intergranular failures and crystals arranged in the direction of the scratches, as can be viewed in Figure 9(b).

By observing the crystal morphology of the plaster in the detrital sections, it was not difficult to see that the plaster in the uniform loading test had been affected by tensile stress, and the crystals had become separated from each other. The crystals were found to be long columnar, loose, and disordered, with obvious pores distributed on the surfaces (Figure 10(a)), which had indicated obvious splitting failures. Under the influences of the compressive stress on the plaster in the gradient loading test, the crystals were found to be staggered with each other, and the crystals were arranged in the same direction in short rod-like shape (Figure 10(b)). Also, there were obvious scratches on the surfaces, which indicates that the rock-burst had produced shear failures. Therefore, macroscopically speaking, it could be reflected that splitting failures had occurred during the uniform loading test, and shear failures had occurred during the gradient loading test.

It was found in this study that the mesoscopic morphology of the detrital sections had accurately reflected the macroscopic failures of the rock-burst, which also indicated that the stress loading modes had affected the failure modes of the specimens to some extent. Therefore, the mesoscopic morphology of the detrital sections had characterized the macroscopic failures of the rock-burst and had also reflected the incubation processes of the rock-burst to a certain extent.

3.2. SEM Image Processing and Fractal Features of the Rock-Burst Detrital Sections

3.2.1. Image Processing Using SEM. The SEM images were able to reflect the mesoscopic morphology and structural characteristics of the plaster crystals under stress conditions. The image processing software was used in this study to extract the crystal contours, and the fractal dimension was calculated by combining the fractal theory. The rock mass failure characteristics under two gradient stress loading conditions could then be quantitatively analyzed.

In the current study, SEM images of 500, 1500 times magnification were obtained using the SEM method. Then, in order to observe and calculate the crystal distribution characteristics more clearly, an image with typical failure characteristics was selected for each numbered sample at different magnifications. The original SEM image was edited using MATLAB software in order to extract the crystal edge contours. Then, the irrelevant information in the image was removed for the purpose of obtaining a crystal contour image. Finally, the image binarization was carried out in order to facilitate the calculations. The specific operation selected a local part of gradient loading test sample No. 4 (with a magnification of 1500) as an example. The original image was a grayscale image. However, after extracting the boundary contours, denoising, and binarization, the following images were obtained (Figure 11).

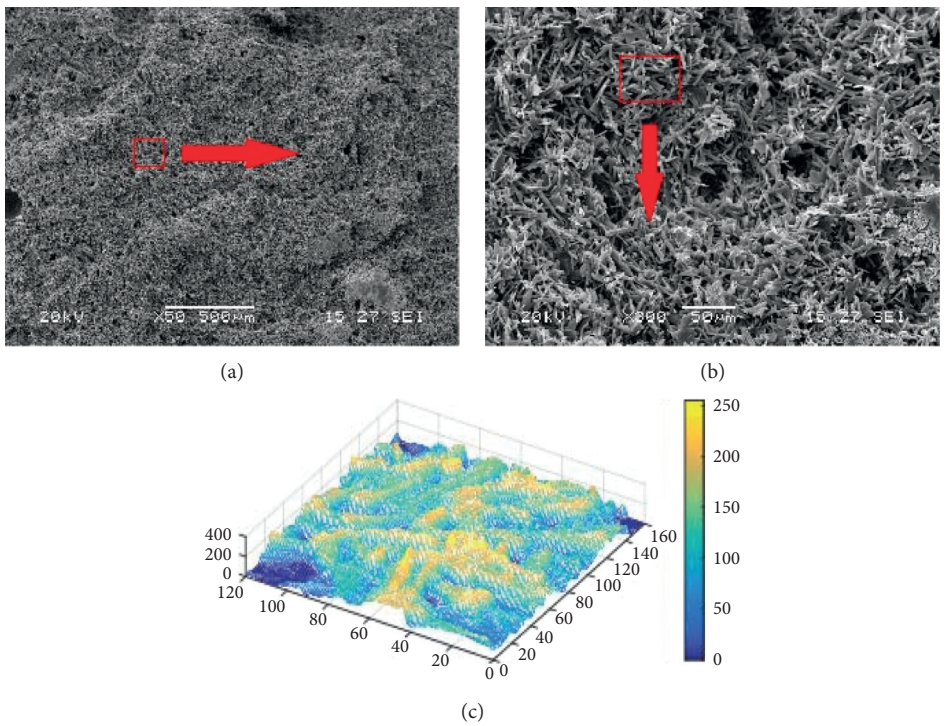

Figure 8: Uniform loading detrital sections: (a) 50x magnification; (b) 300x magnification; (c) 3D profile.

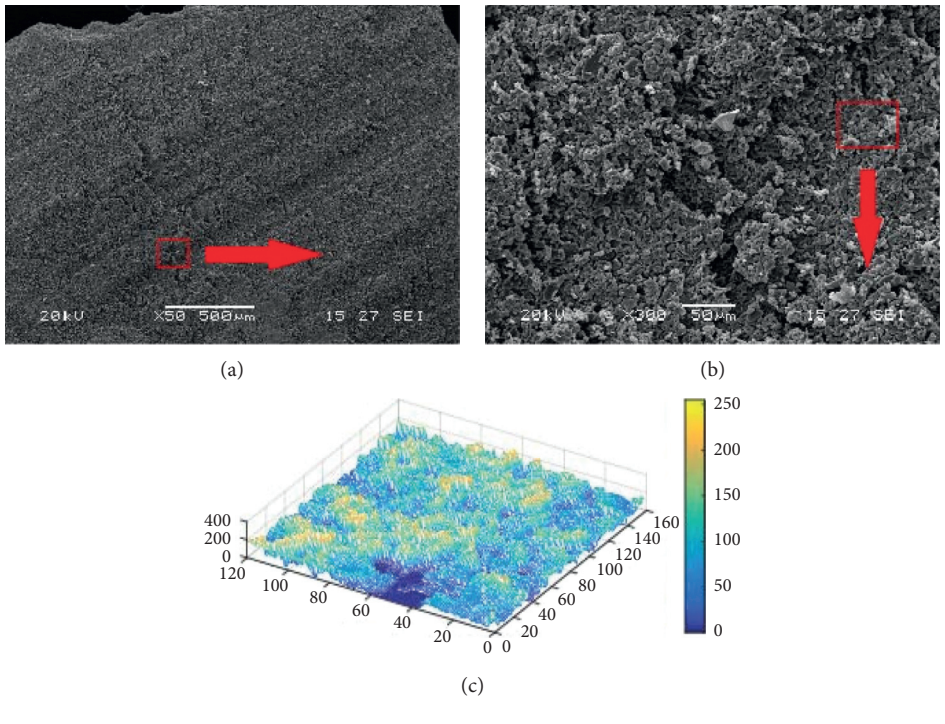

Figure 9: Gradient loading detrital section: (a) 50x magnification; (b) 300x magnification; (c) 3D profile.

The images of the remaining two groups of tests at different magnification were processed in accordance with the same method in order to calculate the fractal dimensions.

3.2.2. Calculations of the Fractal Dimensions of the Crystal Contours. The calculation methods which are used for the fractal dimensions include box-counting methods, sandbox

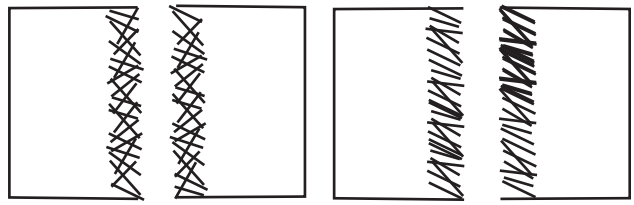

(a) (b)

Figure 10: Schematic diagram of the crystal morphology: (a) uniform loading test; (b) gradient loading test.

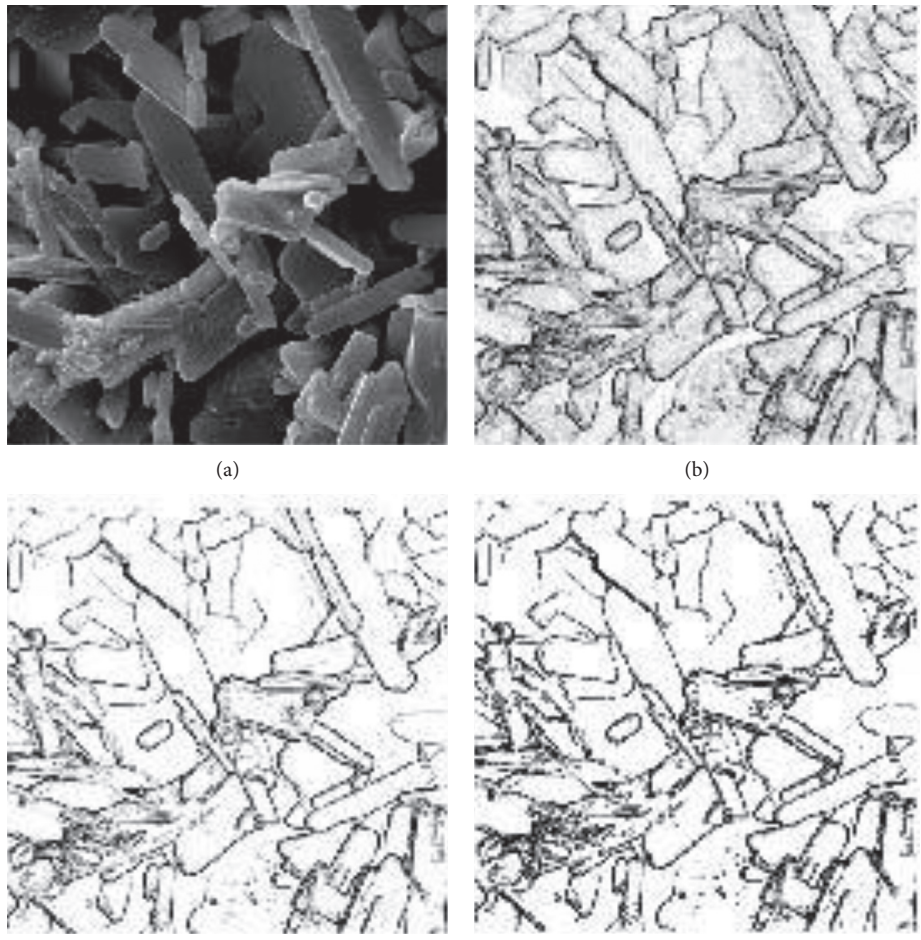

(a) (b)

(c) (d)

Figure 11: Local image processing of sample No. 4: (a) local electron microscopy of sample No. 4; (b) crystal boundary contour diagram; (c) denoised image of the contour image; (d) denoised binary image.

methods, areal-radius methods, and correlation function methods. In this experimental study, the most commonly used box-counting method was applied, as shown in Figure 12. It was assumed that the figure contained multiple crystals, and the square grid of size ε was covered on the contour curve image, and the number of grids intersecting with the contour lines in the statistical grid was $N(\varepsilon)$.

Then, by reducing the size ε and calculating the number of grids intersecting the contour again, it was found that as ε approached 0, the fractal dimension could be obtained as follows:

$$D = \lim_{\varepsilon \longrightarrow 0} \frac{\log N(\varepsilon)}{-\log(\varepsilon)}. \quad (1)$$

It can be known in (1) that the denser the crystal distribution was, the more the crystal contour lines within the unit area would be; also, more boxes would be covered, and the D value would be greater. However, in practice, only the effective side length can be taken, and the specific steps are as follows. Use the side lengths of 512, 256, 128, . . ., 2, 1 square boxes to cover the contour curve image, the size of the different size boxes, and the number of corresponding boxes

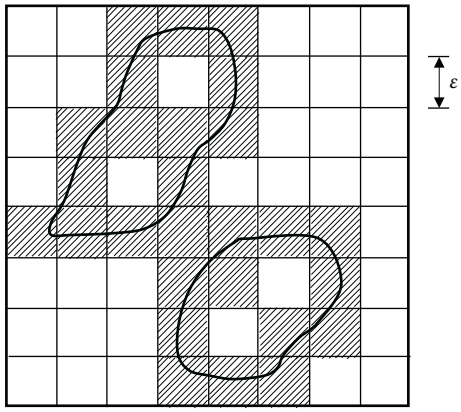

Figure 12: Fractal dimension algorithm of the crystal contours.

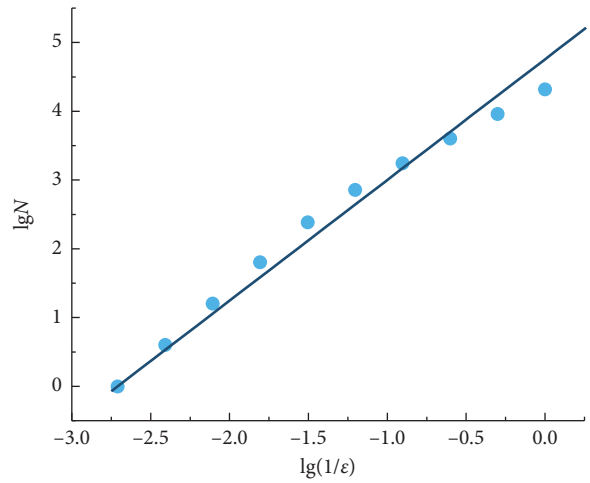

Figure 13: Fractal dimension curve of the crystal contour in gradient test sample No. 4.

N. Therefore, the following equation should be fitted according to a least square method:

$$\lg N(\varepsilon) = D \times \lg\left(\frac{1}{\varepsilon}\right) + C, \tag{2}$$

where C = the fixed coefficient.

The slope D of the line in (2) is the fractal dimension value of the image. Then, according to the aforementioned principles, the corresponding box dimension fractal program can be written in MATLAB, and the relationship diagram of lg$N$ and lg(ε) can be drawn in the logarithmic coordinate system. Figure 13 shows the fractal dimension diagram of the gradient test sample image No. 4. The slope of the fitting curve in the figure is 1.7555. Therefore, the fractal dimension is 1.7555.

The fractal dimensions of crystal contours with two stress loading paths and magnifications were calculated in accordance with the same method by the image processing, as detailed in Table 3.

In the current study, the uniform loading test image samples were denoted by A1, A2, A3, A1, A2, and A3, and the gradient loading test images samples were denoted by B1, B2, B3, B1, B2, and B3. In order to eliminate the interference of multiple factors and also increase the accuracy of the results, three different measurement points were selected from each sample to calculate the average values as the final calculation results.

As can be seen in Table 3, the contours of the plaster crystals had obvious fractal characteristics, and the fractal dimensions had ranged from 1 to 2. It was observed that the larger the fractal dimension is, the more the crystals had aggregated within a certain range. These results indicated that the fractal dimensions of the crystal contour curve were sensitive to the crystal distributions. Therefore, the fractal dimensions obtained by the different loading methods and sampling locations had varied.

3.2.3. Relationship between the Fractal Dimensions of the Plaster Crystal Contours and the Rock-Burst Failure Characteristics. Figure 14 shows line graphs of the mean of the sample fractal dimensions obtained from Table 3 according to the different magnification multiples. It can be seen that when the magnification was 1500 times, the average fractal dimension of the crystal contours obtained by the uniform loading test had ranged between 1.58 and 1.64. Meanwhile, the average fractal dimension of the crystal contours obtained by the gradient loading test had ranged between 1.74 and 1.80. When the magnification was 500 times, the average fractal dimension of the crystal contours obtained by the uniform loading test ranged between 1.79 and 1.84, and the average fractal dimension of the crystal contours obtained by the gradient loading test had been between 1.86 and 1.96. Therefore, it was not difficult to draw the conclusion that, at the same magnification, the fractal dimensions of the gradient loading test samples were greater than those of the uniform loading test samples. That is to say, the fractal dimensions of the crystal contours of the shearing failure detrital sections were greater than those of the splitting failure detrital sections.

In the current experimental study, from the perspective of the failure characteristics of the rock-burst, it was determined that splitting failures had mainly occurred during the uniform loading test. It was observed that, under the actions of the tensile stress, the crystals had been pulled apart in the specimens. Therefore, the crystal edges and corners had become obvious, and the majority of the crystals were found to be intact. During the gradient loading test, it was determined that shear failure was the main failure mode. It could be seen in the test results that, due to the relative shear slip, the detrital section had produced scratches along the movement direction, and the crystal direction had also changed. It was observed that when there was a certain angle between the crystal planes and the shear planes, the crystals had been squeezed and cut off. As a result, the edges and corners were ground down, resulting in powder covering the surfaces, and the detrital section had become dense. The results showed that the compactness of the crystal in gradient loading test was higher than that in uniform loading test. Therefore, it had been confirmed in this study that the fractal dimensions of the crystal contours could reflect not only the tightness

Table 3: Fractal dimensions of the crystal profiles of the rock-burst contour sections with different loading modes and magnification rates.

Loading method	1500x magnification	Fractal dimension	Average	500x magnification	Fractal dimension	Average
Uniform loading	A1	1.6034	1.5835	a1	1.768	1.7904
		1.6008			1.8152	
		1.5463			1.7879	
	A2	1.6006	1.6358	a2	1.8418	1.84
		1.6548			1.855	
		1.6519			1.8233	
	A3	1.5894	1.5869	a3	1.8014	1.7967
		1.5888			1.8007	
		1.5826			1.7881	
Gradient loading	B1	1.7689	1.7692	b1	1.8861	1.8946
		1.7832			1.8964	
		1.7555			1.9014	
	B2	1.7293	1.7427	b2	1.8327	1.8618
		1.7714			1.8732	
		1.7273			1.8796	
	B3	1.7919	1.7991	b3	1.9438	1.952
		1.812			1.949	
		1.7933			1.9632	

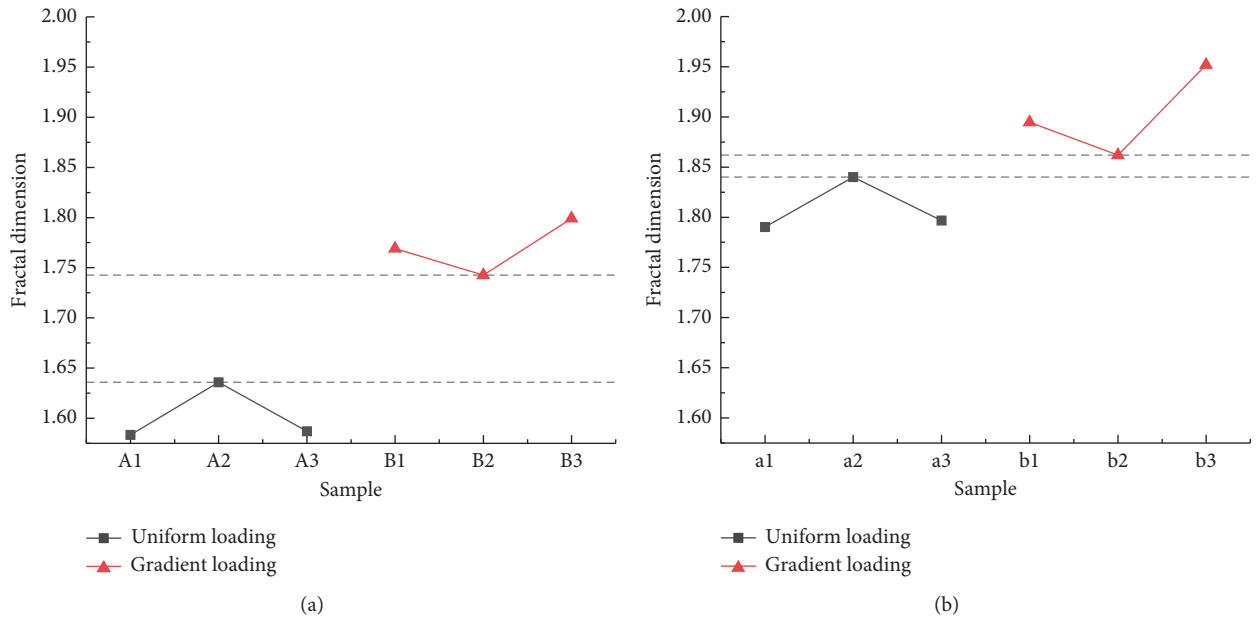

Figure 14: Mean of the fractal dimension of the two groups of test samples: (a) 1500x magnification; (b) 500x magnification.

between the detrital section crystals, but also the failure characteristics of the rock-burst.

3.2.4. Effects of the Magnification Levels on the Fractal Dimensions of the Plaster Crystal Contours. In order to analyze the effects of the magnification levels on the mesoscopic fractal of the plaster specimens, a comparison was made between the data shown in Figure 14. The comparison results indicated that the average fractal dimension of the crystal contours at the 1500x magnification level had ranged from 1.58 to 1.1.64 under the uniform loading conditions. The average fractal dimension of the crystal contours at the 500x magnification level had ranged from 1.79 to 1.84. Therefore, the results at 500x magnification were larger than those at the 1500x magnification level. It was also determined that, under the conditions of the gradient loading, the average value of the fractal dimension of crystal contours at the 1500x magnification level had ranged from 1.74 to 1.80, and the average value of the fractal dimension of the crystal contour at the 500x magnification level had ranged from 1.86 to 1.96. Therefore, the results at 500x magnification were larger than those at 1500x magnification. These results indicated that, with the increases in magnification, the scanning range of the electron microscope had become smaller; the observed crystal structures had become clearer; and the number of crystals within the unit area had decreased, resulting in reductions in the fractal dimensions.

In addition, Points A2 and B2 were represented by two dotted lines parallel to X-axis, as shown in Figure 14. The distance between the dashed lines represented the differences in the range of fractal dimensions between the two groups of tests. At the magnification factor of 1500, the dotted line distance in Figure 14(a) was determined to be 0.1069. At the magnification factor of 500, the dotted line distance in Figure 14(b) was 0.0218. Therefore, since 0.1069 was greater than 0.0218, this indicated that when the amplification factor was 1500, there was a clear degree of differentiation in the fractal dimension range of the two groups of tests, and the different failure characteristics caused by rock-burst could more easily and clearly be distinguished.

4. Conclusions

In this experimental study, an SEM method was used to study the mesoscopic morphological characteristics of rock-burst detrital sections of the rock similar material. The differences in the mesoscopic fracture modes of rock-burst detrital sections of the rock similar material under both uniform loading and gradient loading conditions were qualitatively and quantitatively described for the purpose of explaining the observed differences. The main conclusions which were drawn in this study were as follows.

(1) It was found that the rock-burst characteristics of the plaster specimens under the two gradient stress loading conditions were different. The rock-burst which had occurred during the uniform loading test ($b = 0$) was determined to produce mainly splitting failures. Meanwhile, when the stress gradient coefficient ($b = 6$) in the text was used, the rock-burst which occurred during the gradient loading test was found to produce mainly shear failures.

(2) The mesoscopic morphology of the specimens had accurately reflected the macroscopic failures. It was observed that the plaster specimens could effectively reflect the plastic deformation processes which occur during rock-burst failure processes. As a result, the relationship between the mesoscopic morphology and macroscopic failures could be determined by combining the two gradient stress processes.

(3) The crystal contours of the detrital sections were found to have fractal characteristics, and the different fractal dimensions of the sections had reflected the different failure characteristics of the rock-burst debris. During this study rock-burst testing processes, with plaster used as the rock similar material, it was determined that, under the same magnification factors ($500x$ or $1500x$), the fractal dimensions of the crystal contours of the splitting failure detrital sections during the uniform distribution test were smaller than those observed in the gradient test. In other words, the fractal dimensions of the splitting failure mode were smaller than those of the shear failure mode. It was found that, with the increases in magnification, the fractal dimensions had decreased and the crystal morphology had become clearer.

Data Availability

The data used to support the findings of this study are included within the article.

Conflicts of Interest

The authors declare that they have no conflicts of interest.

Acknowledgments

The authors would like to sincerely appreciate the financial support which was provided for this study by the Research Fund for the National Natural Science Foundation of China (nos. 51504167 and 51474159), the Graduate Innovative Fund of Wuhan Institute of Technology (no. CX2018083), the Doctoral Program of Higher Education (no. 20110143110017), the Science Foundation of Wuhan Institute Technology (nos. K201856 and K201617), and the Fundamental Research Funds for the Central Universities (no. 2017-YB-022).

References

[1] B.-G. He, R. Zelig, Y. H. Hatzor, and X.-T. Feng, "Rockburst generation in discontinuous rock masses," *Rock Mechanics and Rock Engineering*, vol. 49, no. 10, pp. 4103–4124, 2016.

[2] G. Su, X. Feng, J. Wang, J. Jiang, and L. Hu, "Experimental study of remotely triggered rockburst induced by a tunnel axial dynamic disturbance under true-triaxial conditions," *Rock Mechanics and Rock Engineering*, vol. 50, no. 8, pp. 2207–2226, 2017.

[3] K. Du, M. Tao, X.-B. Li, and J. Zhou, "Experimental study of slabbing and rockburst induced by true-triaxial unloading and local dynamic disturbance," *Rock Mechanics and Rock Engineering*, vol. 49, no. 9, pp. 3437–3453, 2016.

[4] Q. Zhu and J. Shao, "Micromechanics of rock damage: advances in the quasi-brittle field," *Journal of Rock Mechanics and Geotechnical Engineering*, vol. 9, no. 1, pp. 29–40, 2017.

[5] N. Xie, Q. Z. Zhu, L. H. Xu, and J. F. Shao, "A micromechanics-based elastoplastic damage model for quasi-brittle rocks," *Computers and Geotechnics*, vol. 38, no. 8, pp. 970–977, 2011.

[6] K. Zhao, H. Y. Zhao, and Q. Y. Jia, "An analysis of rockburst fracture micromorphology and study of its mechanism," *Explosion & Shock Waves*, vol. 35, no. 6, pp. 913–918, 2015.

[7] K. Ng, Y. Sun, Q. Dai, and X. Yu, "Investigation of internal frost damage in cementitious materials with micromechanics analysis, SEM imaging and ultrasonic wave scattering techniques," *Construction and Building Materials*, vol. 50, pp. 478–485, 2014.

[8] D. Q. Wang, M. L. Zhu, and F. Z. Xuan, "Experimental study of fatigue crack initiation and strain evolution around a micro-void by in situ SEM and digital image correlation," *Key Engineering Materials*, vol. 754, pp. 75–78, 2017.

[9] R.-L. Shan, L.-W. Song, Y. Liu, W.-F. Zhao, and H.-X. Chen, "Microstructure analysis of deep rock in Meilinmiao mine," *Journal of Coal Science and Engineering (China)*, vol. 19, no. 4, pp. 468–473, 2013.

[10] M. Zhang, J. G. Ning, H. B. Zhang, and X. S. Liu, "Study on microscopic structure and mineral composition of shallow rock using SEM," *Applied Mechanics and Materials*, vol. 303–306, pp. 2552–2558, 2013.

[11] M. Parsa, A. Maghsoudi, and R. Ghezelbash, "Decomposition of anomaly patterns of multi-element geochemical signatures in Ahar area, NW Iran: a comparison of U-spatial statistics and fractal models," *Arabian Journal of Geosciences*, vol. 9, no. 4, p. 260, 2016.

[12] A. Fujimura, M. Furumoto, Y. Takagi, and H. Mizutani, "Fractal dimensions of fracture surfaces of rock fragments," *National Institute of Polar Research Memoirs*, vol. 41, pp. 348–357, 1986.

[13] P. Wang, Z. Qu, and Y. Cui, "Fractal study for micro-crack of mud-shale," *Key Engineering Materials*, vol. 719, pp. 28–32, 2016.

[14] Y. Deng, M. Chen, Y. Jin, and D. Zou, "Theoretical analysis and experimental research on the energy dissipation of rock crushing based on fractal theory," *Journal of Natural Gas Science and Engineering*, vol. 33, pp. 231–239, 2016.

[15] D. Liu, D. Li, F. Zhao, and C. Wang, "Fragmentation characteristics analysis of sandstone fragments based on impact rockburst test," *Journal of Rock Mechanics and Geotechnical Engineering*, vol. 6, no. 3, pp. 251–256, 2014.

[16] Y. Wang, Z. Chun, M. C. He, D. Liu, Y. Lin, and S. Du, "Fragmentation characteristics analysis of sandstone fragments for impact rockburst under different dynamic loading frequency," *Geotechnical and Geological Engineering*, vol. 37, no. 4, pp. 2715–2727, 2019.

[17] D. J. Li, X. N. Jia, J. L. Miao, M. C. He, and D. D. Li, "Analysis of fractal characteristics of fragment from rockburst text of granite," *Chinese Journal of Rock Mechanics and Engineering*, vol. 29, no. 1, pp. 3280–3289, 2010.

[18] H. Zhou, R. C. Xu, J. J. Lu, C. Q. Zhang, F. Z. Meng, and Z. Shen, "Study on mechanism and physical simulation experiment of slab buckling rockburst in deep tunnel," *Chinese Journal of Rock Mechanics and Engineering*, vol. 34, no. 2, pp. 3658–3666, 2015.

[19] B. Dai, G. C. He, and Z. J. Zhang, "A numerical research on crack process of gypsum containing single flaw with different angle and length in uniaxial loading," *Shock and Vibration*, vol. 2018, Article ID 2968205, 16 pages, 2018.

[20] Y. Y. Xia, L. M. Qin, L. L. Liao, W. Xiong, and Z. D. Wang, "Fractal characteristic analysis of fragments from rockburst tests of large-diameter specimens," *Chinese Journal of Rock Mechanics and Engineering*, vol. 33, no. 7, pp. 1358–1365, 2014.

[21] A. K. Singh, R. Singh, J. Maiti, R. Kumar, and P. K. Mandal, "Assessment of mining induced stress development over coal pillars during depillaring," *International Journal of Rock Mechanics and Mining Sciences*, vol. 48, no. 5, pp. 805–818, 2011.

[22] M. C. He, G. X. Yang, J. L. Miao, X. N. Jia, and T. T. Jiang, "Classification and research methods of rockburst experimental fragments," *Chinese Journal of Rock Mechanics and Engineering*, vol. 28, no. 8, pp. 1521–1530, 2009.

[23] Y. A. Tian, "SEM analysis of rock fracture and progressive failure process of rock burst," *Journal of Electronic Microscopy*, vol. 2, pp. 41–48, 1989.

[24] Y. Yuan, P. Z. Pan, S. K. Zhao, B. Wang, and G. H. Song, "The failure process of marble with filled crack under uniaxial compression based on digital image correlation," *Chinese Journal of Rock Mechanics and Engineering*, vol. 37, no. 2, pp. 339–351, 2018.

[25] C. Y. Liang, S. R. Wu, and X. Li, "Research on micro-meso characteristics of granite fracture under uniaxial compression at low and intermediate strain rates," *Chinese Journal of Rock Mechanics & Engineering*, vol. 34, no. s1, pp. 2977–2986, 2015.

[26] Y. P. Liu, H. Deng, and R. Q. Huang, "Mechanical test of slab-rent structure rock and mesoscopic morphology analysis of rupture surface," *Chinese Journal of Rock Mechanics & Engineering*, vol. 34, no. s2, pp. 3852–3861, 2015.